

Equilibration near the liquid-vapor critical point in microgravity

R. Allen Wilkinson,¹ G. A. Zimmerli,² Hong Hao,³ Michael R. Moldover,⁴ Robert F. Berg,⁴ William L. Johnson,⁵ Richard A. Ferrell,³ and Robert W. Gammon⁶

¹*Microgravity Science Division, NASA Lewis Research Center, Cleveland, Ohio 44135*

²*NYMA Incorporated, 2001 Aerospace Parkway, Brook Park, Ohio 44142*

³*Department of Physics, University of Maryland, College Park, Maryland 20742*

⁴*Physical and Chemical Properties Division, NIST, Gaithersburg, Maryland 20899*

⁵*Department of Physics, Westminster College, New Wilmington, Pennsylvania 16172*

⁶*Institute for Physical Science and Technology, University of Maryland, College Park, Maryland 20742*

(Received 28 March 1997)

We used interferometry to measure the density changes associated with the late stage of thermal equilibration near the liquid-vapor critical point of SF₆. This experiment was performed on board the Space Shuttle in the absence of the considerable obscuring effects of gravity. The density changes were analyzed in terms of the exponentially decaying modes predicted by a model for heat diffusion in an isothermal container. The time constants depended only on the temperature and not on the sample's history. In the temperature range from $T_c + 98$ mK to $T_c + 28$ mK, where $T_c = 319$ K is the critical temperature, the values of the thermal diffusivity D_T derived from the time constants at each temperature are consistent with the values of D_T found by previous dynamic light-scattering measurements. From $T_c + 9$ mK to $T_c + 1.4$ mK, where Earth-based measurements of D_T are unavailable, the measured values of D_T agree with an asymptotically correct extrapolation of D_T closer to T_c . These data confirm our understanding of thermal equilibration in a range of $T - T_c$, where measurements on Earth are severely influenced by gravitationally induced convection and stratification of the sample. [S1063-651X(97)03512-5]

PACS number(s): 47.27.Te, 64.60.Ht, 66.10.Cb

I. INTRODUCTION

In an inviscid fluid, the equation for transport of entropy per unit mass s is

$$\rho T \left(\frac{\partial s}{\partial t} + \nabla s \cdot \mathbf{v} \right) = \nabla \cdot (\lambda \nabla T), \quad (1.1)$$

where ρ , T , λ , and v , are the fluid's density, temperature, thermal conductivity, and velocity, respectively. If v is small, Eq. (1.1) reduces to

$$\dot{T} - \left[1 - \frac{c_V}{c_P} \right] \left(\frac{\partial T}{\partial P} \right)_P \dot{P} = \frac{1}{\rho c_P} \nabla \cdot (\lambda \nabla T), \quad (1.2)$$

where P is the pressure, and c_P and c_V are the heat capacities per unit mass at constant pressure and volume [1]. (See also Refs. [2,3].)

Near the liquid-vapor critical point, the second term of Eq. (1.2) dramatically affects the observed thermal equilibration of fluids. In a typical experimental cell, the interior fluid's temperature closely follows a sudden change of the boundary's temperature. This effect can be understood by examining the solutions to Eq. (1.2), which predict that thermal equilibration has an early, rapid stage as well as a later, slow stage. The early stage lasts only a few seconds, and leaves the near-critical fluid with an inhomogeneous temperature distribution that is close to the new boundary temperature. The early stage of equilibration is rapid because, when the boundaries are heated, the density of the fluid near the boundary rapidly decreases, and fluid expands away from the boundary. This expansion has been called the "piston

effect;" it adiabatically compresses the interior fluid and raises its temperature. The early stage has nonexponential time dependence; thus it cannot be characterized by a single time constant. The existence of the early, rapid stage, whimsically called "critical speeding up," has been confirmed experimentally [4-9].

In the later, slow stage of thermal equilibration, the solutions of Eq. (1.2) are modes which decay exponentially in time toward the boundary's temperature. For a fluid contained in a cylinder with isothermal walls of radius R and height $2z_0 \ll R$, the largest time constant of Eq. (1.2) is

$$\tau = \frac{4z_0^2}{\pi^2 D_T} \left[1 + O\left(\frac{z_0}{R}\right)^2 \right]. \quad (1.3)$$

At the critical density, the thermal diffusivity $D_T = \lambda / (\rho c_P)$ approaches zero as T approaches the critical temperature T_c , and this lengthens greatly the time scale for the final slow approach to equilibrium.

The experiment reported here is the first to demonstrate quantitatively the relevance of Eq. (1.2) to the late stage of equilibration. It was performed on board the Space Shuttle to eliminate the considerable complications caused by gravity. After inducing density gradients in a near-critical sample of SF₆ (sulfur hexafluoride), we used interferometry to observe the subsequent evolution of the density distribution. The evolution was analyzed with Eq. (1.2). Above $T_c + 20$ mK, our results are consistent with values of D_T that had been determined with conventional light-scattering measurements. Below $T_c + 20$ mK, this experiment can be interpreted as a novel measurement of D_T . The new values of D_T , obtained

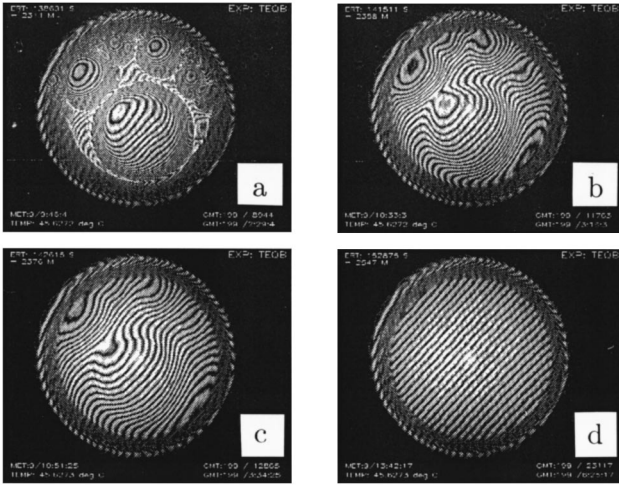


FIG. 1. A typical sequence of interferograms during equilibration. In event o the sample was heated from $T_c - 50$ mK to $T_c + 8.4$ mK, and then allowed to equilibrate. (a) Immediately after the thermostat had stabilized at $T_c + 8.4$ mK, the regions of differing density are remnants of the mm-sized regions of liquid and vapor that were present at $T_c - 50$ mK. (b) 47 min after the first frame, the fringes are continuous. This frame's time was defined as $t=0$ for the analysis of event o . (c) 65 min after the first frame. (d) 236 min after the first frame.

as much as 15 times closer to T_c than heretofore, are in agreement with a theoretically-based extrapolation of the Earth-based values.

An example of the slow equilibration of density can be seen in Fig. 1. The sample's temperature was initially $T_c - 50$ mK, where it had separated into mm-sized liquid and vapor regions. After heating above T_c , these regions slowly merged into a homogeneous fluid. The first interferogram was recorded immediately after the thermostat's temperature had stabilized at $T_c + 8.4$ mK, and the last interferogram was recorded after the sample had become nearly homogeneous. (The fringes in the last interferogram were caused by a deliberate mirror tilt in the reference leg of the Twyman-Green interferometer.) All of the interferograms at intermediate times show density inhomogeneities. Even though the sample was only 1 mm thick and 10 mm in diameter, equilibration was characterized by a time constant of approximately 2400 s.

The temperature gradient which remained after the early stage relaxation was comparatively small. (For example, ~ 10 μ K/mm in Fig. 1.) However, the associated density gradient was large enough to be measured easily because $(\partial\rho/\partial T)_P$ diverges strongly as $T \rightarrow T_c$. We measured this density relaxation at late times, where the time dependence was expected to be exponential.

In contrast with the present experiment, studies of the equilibration of near-critical fluids in the Earth's gravity have not yielded results in agreement with models for the experiment. Earth-based tests of Eq. (1.2) are inherently more complex than the present experiment. Equation (1.2) assumes that the effects of convection are negligible. On Earth, it is extraordinarily difficult to suppress buoyancy-driven convection as the critical point is approached because the thermal expansion coefficient (which drives convection)

diverges and because the thermal diffusivity (which suppresses convection) approaches zero. In microgravity, even when convection is present, convective heat transport and velocities are greatly reduced. On Earth, one must also account for significant stratification of the sample in the Earth's gravity [10].

A recent, careful study of the equilibration of near-critical ^3He on Earth [6] chose a geometry designed to minimize the effects of convection and accounted for stratification in modeling the experiment. Nevertheless, as T_c was approached, the measured equilibration time constants were as much as a factor of 10 shorter than the calculated equilibration time constants. A likely cause of the discrepancies was undesired conduction through the sample cell's side walls [11]. Recent measurements in an improved cell subjected to low-frequency temperature oscillations found much better agreement with the calculated response of the fluid [12].

The present measurements of the later, slow stage complement prior studies of the earlier, rapid stage of equilibration [4–9]. Together, they confirm that Eq. (1.2) describes the thermal equilibration of near-critical pure fluids in microgravity. This understanding can be used to optimize the design of future critical point experiments in microgravity, and also to reinterpret the data from experiments that have been completed. As an example, we mention CVX [13], an experiment designed to measure the viscosity near the critical point of xenon on board the Space Shuttle in July 1997. At $T_c + 0.6$ mK, the comparatively large sample will have a thermal equilibration time of 28 days, greater than the 12-day length of the Shuttle mission. However, meaningful data will be taken under these constraints because the sample will be brought sufficiently close to its equilibrium state by a temperature ramp that exploits the rapid attainment of near-equilibrium predicted by Eq. (1.2).

In this paper, we report measurements of the approach to equilibrium in microgravity, and compare our data to a model based on Eq. (1.2). Section II describes our model, Secs. III and IV the experimental method, Sec. V the analysis technique, and Section VI our results. Section VII concludes the paper.

II. THEORETICAL MODEL

To predict the approach to equilibrium, we used an idealized model that, in part, can be solved analytically. The model assumes that the fluid's temperature differences δT and density differences $\delta\rho$ are sufficiently small,

$$\delta T \ll (T - T_c) \quad \text{and} \quad \delta\rho \ll \rho_c, \quad (2.1)$$

and that the fluid's heat capacity and thermal conductivity are independent of position and time. In a closed container of volume V , this allows Eq. (1.2) to be approximated by [1–3]

$$\dot{T} - \frac{1}{V} \left[1 - \frac{c_V}{C_P} \right] \int \dot{T} dV = D_T \nabla^2 T. \quad (2.2)$$

Equation (2.2) is valid when pressure is a function of time but not position, at times much greater than the container's time scale for sound damping.

Equations (1.2) and (2.2) have solutions which decay exponentially at long times. (At short times, the solutions can

TABLE I. Reduced time constants of the eight slowest isobaric modes.

Mode (ab)	$(\pi^2 D_T / 4z_0^2) \tau_{ab}$ for $z_0/R=0.1$
(11)	0.9402
(21)	0.8904
(31)	0.8323
(12)	0.8309
(41)	0.7703
(51)	0.7076
(32)	0.7029
(13)	0.7025

decay rapidly from their initial amplitudes by more than a factor of 100.) The model approximated the boundaries of the fluid volume as a hollow isothermal disk of thickness $2z_0 = 1$ mm and radius $R = 5$ mm. In a geometry of such high symmetry, these solutions can be classified into nonisobaric and isobaric modes [14]. The isobaric modes ($\dot{P}=0$) are those for which the integral term in Eq. (2.2) vanishes due to the antisymmetry of $T(\mathbf{x})$; thus they are the same modes as those of the simple equation

$$\dot{T} = D_T \nabla^2 T. \quad (2.3)$$

In a disk, part of the temperature deviation δT can be written as a sum of the slower isobaric modes,

$$\begin{aligned} \delta T(r, \theta, z, t) = & \sum_{a=1}^{\infty} \sum_{b=1}^{\infty} [A_{ab} \sin(a\theta) \\ & + B_{ab} \cos(a\theta)] \cos(qz) J_a(k_{ab}r) e^{-t/\tau_{ab}}, \end{aligned} \quad (2.4)$$

where r , θ , and z are the radial, angular, and thickness coordinates, J_a is the Bessel function of order a , and $k_{ab}R \equiv j_{ab}$ is the b th root of the equation $J_a(j_{ab})=0$. Faster-decaying solutions proportional to $\sin(nqz)$ and to $\cos(nqz)$, with $n > 1$, are not considered here. The isothermal boundary condition $\delta T=0$, determines the wave vectors q and k_{ab} through

$$qz_0 = \frac{\pi}{2} \quad \text{and} \quad J_a(k_{ab}R) = 0. \quad (2.5)$$

The corresponding time constants are

$$\tau_{ab} = \frac{4z_0^2}{\pi^2 D_T} \left[1 + \frac{4(j_{ab}^2 + a^2)}{\pi^2} \left(\frac{z_0}{R} \right)^2 \right]^{-1}. \quad (2.6)$$

Many of these time constants have nearly identical values. As shown in Table I for our aspect ratio of $z_0/R=0.1$, the time constants of the four slowest isobaric modes differ by less than 14%. A subsequent paper [15] contains a discussion of the relative strengths to be expected for the various modes.

The complete solution of Eq. (2.2) also includes nonisobaric modes, which do not have a known closed form in two and three dimensions. The nonisobaric modes are orthogonal to the isobaric modes. In principle they may be omitted from

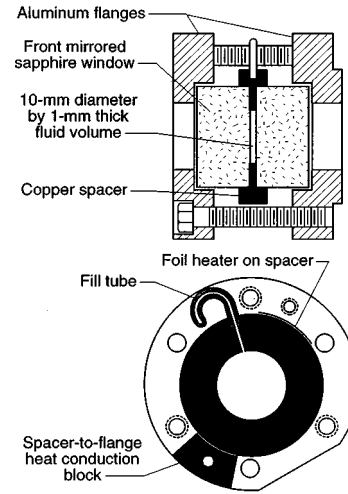


FIG. 2. Two views of the interferometer sample cell.

the model without affecting the amplitudes of the isobaric modes deduced from fitting the interferograms.

Nevertheless, we added to the sum Eq. (2.4) the function

$$f_0(r) \equiv J_0(k_{01}r) - \langle J_0(k_{01}r) \rangle, \quad (2.7)$$

to approximate the slowest nonisobaric mode. Here, the brackets $\langle \rangle$ denote an average over the disk of radius R . The function $f_0(r)$ is not a solution of Eq. (2.2); however, numerical studies verified that $f_0(r)$ is a good representation of the slowest nonisobaric mode, and it obeys conservation of mass. Some further theoretical aspects are presented in a subsequent paper [15].

III. APPARATUS

A. Sample cell

The experimental cell is sketched in Fig. 2. Most of the fluid sample was contained in a coin-shaped volume of 75 mm^3 bounded by two cylindrical sapphire windows and by a circular copper spacer. The volume had a diameter of 10.0 mm and an axial thickness of 0.96 mm. This small thickness was chosen to limit the longest relaxation time to a few hours. Also, the interferometry required a small thickness because of the sample's large turbidity near T_c . The two sapphire windows had electrically conductive, nearly transparent, indium-tin oxide coatings on their inner surfaces, and they were in electrical contact with the copper spacer. Thus electrostatic charges on the sapphire did not influence the fluid. A foil heater was cemented to a 25° sector of the spacer's outside diameter. Diametrically opposite from the heater, a copper block thermally connected the spacer to the cell's aluminum flanges. This orientation of the heater and the heat sink allowed us to heat the spacer, and thus the sample, asymmetrically. When the heater was off, the cell's copper and sapphire walls comprised a very nearly isothermal boundary for the sample.

After careful cleaning of all parts, both windows were sealed against the spacer by gold O rings made from 0.25-mm-diameter gold wire. The entire assembly, consisting of the spacer, O rings, windows, and flanges, was clamped together with six titanium-alloy screws whose thermal expan-

sivity closely matched that of the cell's other components. After final tightening of the screws, the windows were 4.5 fringes from parallel and less than 0.1 fringe from flat. After assembly, the cell was filled with helium to 10 MPa and tested for leaks both at room temperature and at 60 °C. No leaks were found. A leak of 1.5×10^{-9} atm cm³ s⁻¹ could have been detected. The cell was then baked at 100 °C under vacuum for several hours.

To fill the cell with SF₆, a copper fill tube had been vacuum brazed into the side of the spacer. After filling the cell, the tube was sealed by crimping. The sealed tube's volume added 5% to the main volume of 75 mm³. The SF₆ was stated by the manufacturer to be 99.999% pure, with CF₄ and air as the main impurities. To minimize volatile impurities, the SF₆ was drawn from the liquid phase at the bottom of the inverted storage cylinder. Prior to filling, the cell was flushed with gaseous SF₆. Liquid SF₆ was condensed into the cell at 0 °C. The cell was then filled with SF₆, while immersed in a water bath at a temperature just below T_c . The density was adjusted to the critical density by adding or removing SF₆ until the liquid-vapor meniscus was at the proper height. The proper height was determined from a calculation of the average density that accounted for the position and volume of the sealed capillary. When the proper height had been achieved, the fill line was crimped, cut, and soldered at its tip. The final density was measured to be within 0.1% of the critical density.

The distance $2z_0$ between the two sapphire windows of the assembled, filled sample cell was measured using a microscope with a calibrated stage. Measurements were made at four locations at ambient temperature. The result was $2z_0 = (0.957 \pm 0.014)$ mm after correcting for the refractive index [16] of the SF₆. (The uncertainty cited is the standard deviation of the mean.)

B. Thermostat

The cell was mounted inside the sample cell unit (SCU), an aluminum cylinder 115 mm long and 60 mm in diameter. Flush mounting of the aluminum flange faces gave good thermal contact to the SCU. The SCU was the core of a four-shell thermostat which was installed in the critical point facility (CPF) [17]. The CPF provided temperature control for the thermostat. It contained optical components, including light sources, shutters, and video and 35-mm cameras. The CPF coordinated the optical and temperature measurements according to a stored program which was modified by commands uplinked from the ground during the flight. During the flight, the CPF controlled the SCU's temperature using Peltier elements at both ends of the SCU, and a thermistor thermometer mounted near one end of the SCU. This control thermistor had been calibrated with an accuracy of 3 mK against a platinum thermometer [18]. Steady-state temperature gradients within the fluid-filled cells within the SCU were specified to be less than 100 μK cm⁻¹.

Four auxiliary thermistors mounted within the SCU allowed us to monitor the thermostat's performance. During the longest quiescent period, the 6-h interval following event q (see Sec. IV B), the temperature records were approximately linear drifts that varied from +2 to -6 μK per hour, depending on the thermometer. This indicates that the SCU's

temperature gradient had a time dependence of the order of $(dT/dx)_{SCU} = 2 \times 10^{-8}$ K m⁻¹ s⁻¹, where we used 6 cm as a typical distance between thermometers. Superposed on all four temperature records was an unprogrammed upward "step" of approximately 40 μK that occurred near the middle of the quiescent interval. The step was smoothed by a time constant on the order of 10 min, comparable to the thermal response time of the SCU.

C. Interferometer

The sample was illuminated by a 633-nm, collimated, polarized laser beam. Its intensity was 3.3 mW m⁻², and 0.26 μW passed through the sample. The beam splitter and both legs of the Twyman-Green interferometer were housed in the SCU. One leg terminated at a multilayer dielectric mirror coated onto the inner surface of the cell's rear window; thus the light beam traversed the 0.96-mm thickness of the sample twice. The reference leg terminated in a mirror which had been tilted to produce 26 fringes across the diameter of the cell when the sample was homogeneous. A larger tilt would have produced more fringes, giving greater position resolution for small density changes; however, when large density gradients were present, the plethora of closely spaced fringes would not have been resolved. The interferometric images were recorded at six-second intervals by a CCD video camera that digitized with six bits of gray-scale resolution and 512×512 pixels of spatial resolution.

In practice, we restricted our analysis to interferograms with fringe shifts $\Delta N \leq 4$. See Fig. 1. The corresponding fractional density deviation was

$$\frac{\delta\rho}{\rho_c} \approx \frac{\lambda_{\text{laser}}}{l} \left(\rho \frac{dn}{d\rho} \right)^{-1} \Delta N \leq 0.014. \quad (3.1)$$

(Here $l = 2$ mm is the optical path length through the SF₆, λ_{laser} is the laser's wavelength, $n = 1.091$ is the refractive index [16], and the value $\rho(dn/d\rho) = 0.093$ was calculated from the Clausius-Mossotti relation.) The noise in the optical measurement was independent of $(T - T_c)$, and corresponded to approximately $\frac{1}{20}$ fringe. Thus the dynamic range of the density relaxation data was a factor of 80.

The density deviations induced two small optical errors. The refractive index gradient caused the fluid to act as a prism, thus translating the image of the fluid slightly. This translation had little influence on the final analysis. The gradient also changed the optical phase. The resulting distortion of the interferogram was second order in the refractive index gradient, and was negligible [19].

IV. EXPERIMENTAL PROCEDURE

This experiment, denoted thermal equilibration bis (TEQ-B), was carried out during July 1994 in CPF, which was part of the second International Microgravity Laboratory (IML-2) on board Space Shuttle flight STS-65. The average acceleration between infrequent, short thruster firings was of the order of 10^{-6} of Earth's gravitational acceleration.

A. Determination of the critical temperature

The sample's critical temperature was measured three times during the flight by slowly cooling the thermostat, and

TABLE II. Observations of T_c .

Time of phase transition (h:min)	\dot{T} ($\mu\text{K/s}$)	T_c (K)
5:20	-3.3	318.7670
61:04	-3.3	318.7687
72:43	-0.55	318.7689

observing the onset of the extreme turbidity associated with phase separation. Although this criterion was sufficiently precise to locate T_c to within two frames (12 s) of the video tape, corresponding to less than 0.1 mK, Table II shows that the irreproducibility of T_c was much greater. In particular, the first and second measurements of T_c differed by 1.7 mK. We attributed this difference to an anomalous change in the temperature distribution within the SCU during the first measurement. We did not expect such a change because both measurements were made at the cooling rate $\dot{T} = -3.3 \mu\text{K/s}$. Nevertheless, the difference between the control thermometer and the four auxiliary thermometers within the SCU changed by as much as 0.9 mK between the first and second measurements. In contrast, the second and third measurements of T_c differed by only 0.2 mK, even though \dot{T} had been reduced by a factor of 6. This is consistent with the SCU's temperature distribution, which did not change by more than 0.2 mK between the second and third measurements.

For the analysis in this paper, we assigned the value $T_c = 318.7689 \text{ K}$ resulting from the third measurement. The third measurement was chosen because (1) it immediately followed the equilibration closest to T_c , ($T_c + 1.4 \text{ mK}$), (2) it was the most precise measurement, and (3) it agreed with the second measurement to within 0.2 mK.

There is additional, less direct, evidence that it was the first determination of T_c that was anomalous rather than both the second and third determinations. A second sample cell

was present within the SCU during all of the measurements described here. This cell was used for direct visualization of near-critical SF_6 . In most respects the visualization cell was identical with the interferometer cell. In particular, it had been filled with SF_6 from the same supply container as the interferometer cell. For the visualization cell, T_c was determined four times. These four determinations spanned only 0.2 mK, and their average was only 0.2 mK below the average of the second and third determinations of T_c in the interferometer cell.

B. Creation of density inhomogeneities

During the experiment, the sample's density distribution was intentionally disturbed from equilibrium 17 times. Each disturbance was called an "event," and their characteristics are summarized in Table III. We used two procedures to create the density inhomogeneities. In 12 events they were created by applying an electrical pulse to the cell's heater. The pulse temporarily heated the cell's body asymmetrically, thereby producing a nonequilibrium density distribution. Figure 3 is an example of such a distribution. The other five events were created by heating the cell from a temperature below T_c . The preceding two-phase, inhomogeneous distribution of liquid and vapor persisted above T_c as regions of differing density. Figure 1 is an example of such a distribution.

At the highest temperature, $T_c + 198 \text{ mK}$, the sample relaxed faster than the thermostat. Under this condition, the quantitative interpretation of the equilibration measurements requires a detailed thermal model of the SCU, and is of little interest here. At the lowest temperature, $T_c + 1.4 \text{ mK}$, the sample relaxed with an apparent time constant of approximately 4 h. This slow relaxation limited the number of events which could be studied near T_c during the 76 h which were allotted to this experiment.

TABLE III. Characteristics of the 17 density disturbance events.

Event	$(T - T_c)$ (mK)	Temperature history/pulse energy	Duration of analysis (s)
<i>a</i>	198.2	0.59 J/20 s	258
<i>b</i>	198.2	0.59 J/20 s	228
<i>c</i>	98.6	cool from $T_c + 300 \text{ mK}$, 1.03 J/1561 s	2315
<i>d</i>	98.6	2.7 J/5 s	3021
<i>e</i>	98.6	2.4 J/900 s	2686
<i>f</i>	98.4	heat from $T_c - 300 \text{ mK}$, 0.30 J/20 s	2183
<i>g</i>	48.4	heat from $T_c - 1 \text{ K}$	7401
<i>h</i>	28.4	1.41 J/2346 s	7573
<i>i</i>	28.7	0.73 J/10 s	6547
<i>j</i>	28.4	0.28 J/241 s	5306
<i>k</i>	28.4	heat from $T_c - 300 \text{ mK}$	8945
<i>l</i>	8.4	0.32 J/21 s	9551
<i>m</i>	8.6	0.10 J/20 s	11 282
<i>n</i>	8.5	0.28 J/240 s	14 940
<i>o</i>	8.4	heat from $T_c - 50 \text{ mK}$	11 360
<i>p</i>	3.4	0.28 J/240 s	16 848
<i>q</i>	1.4	heat from $T_c - 300 \text{ mK}$ to $T_c + 30 \text{ mK}$, then cool	25 105

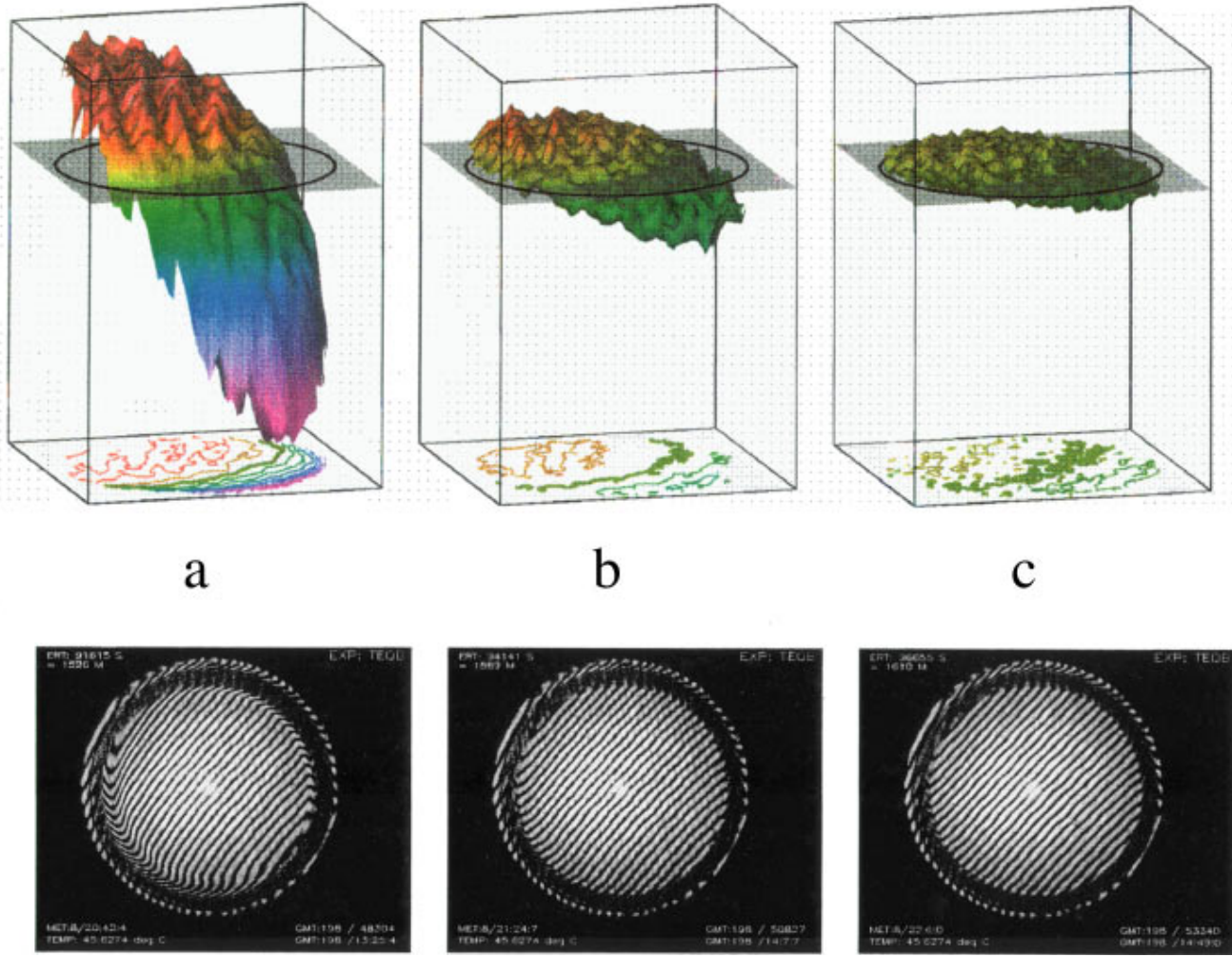


FIG. 3. (Color) A sequence of interferograms and the corresponding net phase maps from event n at $T - T_c = 8.5$ mK. Event n was initiated by an asymmetric heat pulse. The heater's location corresponds to the lower left boundary of the interferograms and the lower right boundary of the phase maps. The net phase was proportional to the local density deviation from equilibrium. Each phase map is represented by both a surface and a contour map. Zero net phase is indicated by the plane surrounding the surface and by the heavy green contour line. The dark circle in the plane represents the cell's boundary. (a) Beginning of the analysis interval ($t = 0$). The contour interval is equal to the 0.2 fringe. (b) Approximately one time constant later ($t = 42$ min). The contour interval is equal to the 0.2 fringe. (c) $t = 84$ min. The contour interval is equal to the 0.1 fringe.

V. DATA ANALYSIS

Our analysis assumed that the observed density deviations $\delta\rho$ were proportional to the temperature deviations δT within the sample. This assumption required the conditions $\delta\rho \ll \rho_c$ and $\delta T \ll (T - T_c)$. The maximum fractional density deviation included in our analysis was $\delta\rho/\rho_c = 0.014$. The δT associated with the density deviation was small. For example, in Fig. 1 at $T_c + 8.4$ mK, the temperature deviation was

$$\delta T \approx \left\{ \frac{T_c}{\Gamma} \left[\frac{T}{P} \left(\frac{\partial P}{\partial T} \right)_\rho \right]^{-1} \right\} \left(\frac{T - T_c}{T_c} \right)^\gamma \left(\frac{\delta\rho}{\rho_c} \right) = 34 \mu\text{K}. \quad (5.1)$$

(Here $\Gamma = 0.046$ and $\gamma = 1.24$ are the amplitude and exponent for the critical susceptibility [10], and $(T/P)(\partial P/\partial T)_\rho$ is the slope of the critical isochore at the critical point [20].) Equations (3.1) and (5.1) confirm that $\delta\rho \ll \rho_c$ and $\delta T \ll (T - T_c)$ throughout the analysis intervals.

The images were analyzed by a multistep procedure, called ‘‘Method 1’’ below. To assess potential systematic errors that might have been introduced by this complex, computer-intensive procedure, we used two additional methods of analysis. All three methods began by choosing an interval of time following an event. The beginning of the analysis interval was defined by two requirements: (1) that the thermostat's temperature was within 0.1 mK of its final value, and (2) that individual interference fringes could be resolved. The analysis ended when the residual fringe shifts were comparable to the measurement's noise. Figure 1(b) is typical of the beginning of an analysis interval, and Fig. 1(d) is typical of the end of an analysis interval.

A. Method 1: Phase difference analysis

For this method, the interferograms were transformed into maps of optical phase as a function of position. A reference map was subtracted from the phase maps to produce a phase difference map. The phase difference maps were projected

onto a subset of the expected spatial eigenfunctions. The time-dependent amplitude of each eigenfunction was fitted by an exponential function to yield the time constant of that eigenfunction.

1. Conversion of interferograms to phase maps

We used commercial software designed for mirror and lens testing [21,22] to process the interferograms. First, the digital image created by CPF was reformatted to be compatible with the commercial software. Then the image was masked to exclude the image of the copper spacer. The software located the centers of the dark fringes to define ordered contours of constant phase. A two-dimensional cubic spline interpolation scheme converted the contours into a phase map consisting of a 64×64 square grid of phase values. We then subtracted a similarly processed reference map representing the nearly homogeneous, equilibrated sample. The reference map had been derived from the last interferogram of the relaxation event, two to five time constants after the event. Figure 3 shows examples of phase difference maps. For the analysis interval following each event, we used approximately 25 images spaced equally in time.

As a check on the accuracy of this conversion, we examined event n (Fig. 3) for correspondences between the qualitative features of the phase maps and of the interferograms. We found two errors. First, early in the analysis interval, the image of the fluid was translated approximately 3% of the cell's diameter along the refractive density gradient. We ignored this translation, and the mask was placed at the boundary of the unrefracted image of the equilibrium fluid. Second, the phase maps in Fig. 3 do not represent accurately the large density gradients which occurred within 5% of the cell's diameter from the cell's boundary. These gradients are visible as hooks at the ends of the fringes in the first two interferograms. Their direction indicates that the fluid's density was nearly uniform at the circular boundary, as expected for a cell with isothermal walls. In contrast, the corresponding phase maps in Fig. 3 do not show gradients corresponding to the hooks near the boundary. Instead, the phase maps show an unexpected smooth azimuthal dependence of the fluid's density at the boundary. This unexpected behavior resulted from the limited spatial resolution of the software that converted interferograms to phase maps. We ignored this error in the phase maps.

Our neglect of these two errors had little effect on the final results because the errors were confined to the edges of the interferogram, while our further analysis, described below, fit smooth functions of position to the entire phase map. We made an independent test of the phase map's ability to characterize the interferogram's broad features. We calculated the spatially averaged phase difference of each map. Ideally, this average would be zero because conservation of mass required that the average density deviation be zero at all times. In fact, the average phase difference was less than 5% of the maximum phase difference, and this is consistent with the limited spatial resolution of the phase map and the fill tube's hidden volume.

2. Fitting to phase maps

The phase difference maps were assumed to be proportional to deviations of density averaged over the cell's thick-

ness. At each time t , a two-dimensional function was fit to the phase difference map in two ways. In Method 1a the map was fit by a sum of Bessel functions,

$$\phi(r, \theta, t) = \tilde{A}_0(t)f_0(r) + \sum_{a=1} \sum_{b=1} [\tilde{B}_{ab}(t)\sin(a\theta) + \tilde{C}_{ab}(t)\cos(a\theta)]J_a(k_{ab}r), \quad (5.2)$$

where $\phi(r, \theta, t)$ is the phase difference in polar coordinates. Thus the time dependence of the density perturbation was described by the coefficients \tilde{A}_0 , \tilde{B}_{ab} , and \tilde{C}_{ab} . We included terms proportional to $J_1(k_{11}r)$, $J_2(k_{21}r)$, $J_3(k_{31}r)$, and $J_1(k_{12}r)$, corresponding to the four slowest expected modes. Usually, due to its large amplitude, terms proportional to $J_1(k_{13}r)$ were also included.

Method 1b was motivated by the observation that the phase maps produced by heating events often resembled a tilted plane whose tilt slowly decreased with time. An initial, nearly planar distribution of fluid density was often created by heating events, as if heating had imposed a linear temperature gradient on the cell's boundary. We expected the cell's boundary to become nearly isothermal within a few minutes after turning off the cell's heater. However, the phase maps displayed long-lived deviations which resembled a tilted plane even near the copper boundary. Therefore the six terms proportional to $J_1(k_{11}r)$, $J_1(k_{12}r)$, and $J_1(k_{13}r)$ were replaced by only two terms proportional to r , representing a tilted plane passing through the origin. The fitting function was then

$$\phi(r, \theta, t) = \tilde{A}_0(t)f_0(r) + \tilde{B}_{\text{tilt}}(t)r \sin(\theta) + \tilde{C}_{\text{tilt}}(t)r \cos(\theta) + \sum_{a=2}^3 [\tilde{B}_{a1}(t)J_a(k_{a1}r)\sin(a\theta) + \tilde{C}_{a1}(t)J_a(k_{a1}r)\cos(a\theta)]. \quad (5.3)$$

The inconsistency between our use of a tilted plane and eigenfunctions consistent with isothermal boundary conditions did not greatly affect the analysis of the fluid's time dependence. This similarity of results is illustrated in Fig. 4, where a tilt is approximated at time $t=0$ by a weighted sum of 100 Bessel functions obeying the boundary condition $\phi(R)=0$. The sum

$$\sum_{b=1}^{100} B_{1b}J_1(k_{1b}r)\exp(-t/\tau_{1b}) \quad (5.4)$$

includes 100 exponential decays, and retains most of its linear character even at $t = \tau_{11}$. This representation shows that an initial condition resembling a linear tilt will retain this appearance even when the boundary condition $\phi(R)=0$ is imposed. An equivalent analytic treatment is presented in a subsequent paper [15].

3. Experimental time constants

In our analysis, each of the amplitudes $\tilde{A}_0(t)$, $\tilde{B}_{ab}(t)$, and $\tilde{C}_{ab}(t)$ in Eqs. (5.2) or (5.3) were fit by adjusting the three parameters K , A , and τ appearing in the function

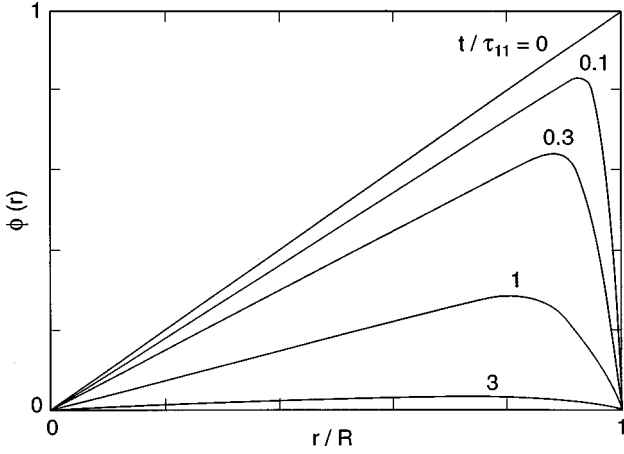


FIG. 4. Modeled evolution of the weighted sum $\sum_{b=1}^{100} B_{1b} J_1(k_{1b}r) \exp(-t/\tau_{1b})$ of 100 Bessel functions obeying the boundary condition $\phi(R)=0$ and chosen to approximate the function $\phi(r)=r \cos(\theta)$ at $t=0$. The sum includes 100 exponential decays, and retains most of its linear character even at $t=\tau_{11}$.

$$K + A[\exp(-t/\tau) - \exp(-t_{\text{ref}}/\tau)]. \quad (5.5)$$

Here $t=0$ was the time of the first image, and t_{ref} was the time of the last image. The last term accounted for the fact that at $t=t_{\text{ref}}$ the sample was not in the true equilibrium that would be achieved at $t=\infty$. The first term K allowed for noise in the reference image; it was always insignificant. As examples, Fig. 5 shows four of the exponential decays associated with event n at $T_c + 8.5$ mK.

In Method 1b, the amplitudes $\tilde{B}_{\text{tilt}}(t)$ and $\tilde{C}_{\text{tilt}}(t)$ were assumed to have the time dependence of an infinite sum of Bessel functions instead of a single exponential decay. The Bessel sum was assumed to be exactly linear in space at the time $t=-t_0$. We therefore fit the time dependence of $\tilde{B}_{\text{tilt}}(t)$ and $\tilde{C}_{\text{tilt}}(t)$ with the four-parameter function

$$K + A \left\{ \exp(-t/\tau_{\text{tilt}}) \exp[-0.287\sqrt{(t+t_0)/\tau_{\text{tilt}}}] - \exp(-t_{\text{ref}}/\tau_{\text{tilt}}) \exp[-0.287\sqrt{(t_{\text{ref}}+t_0)/\tau_{\text{tilt}}}] \right\}, \quad (5.6)$$

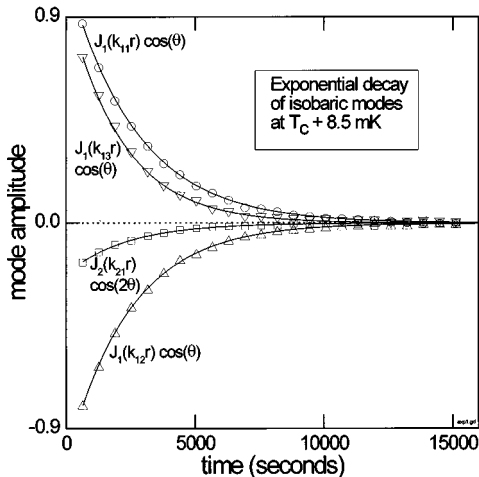


FIG. 5. Time dependence of the amplitudes for several of the modes of event n at $T - T_c = 8.5$ mK. The lines are the best fits to an exponential decay.

which approximates the Bessel sum for early times. The fits were not sensitive to variation of t_0 by a factor of 10; therefore we fixed $t_0 = 1000$ s. The expected value of τ_{tilt} is given by

$$\tau_{\text{tilt}} = 1.047 \tau_{11}. \quad (5.7)$$

An alternative analytic derivation of Eq. (5.6) is presented in a subsequent paper [15].

Table IV lists the time constants τ_{ab} deduced by Method 1a. Two values are listed for each τ_{ab} , one deduced for the mode proportional to $\sin(\theta)$ and the second deduced for the mode proportional to $\cos(\theta)$. The two experimentally derived time constants did not differ in a clear pattern. Also listed is the time constant τ_{tilt} deduced by Method 1b, and the time constant τ_0 that characterized the relaxation of the slowest nonisobaric mode. For some events, either the spatial fit or the temporal fit was poor. In such cases, τ_{ab} was omitted from the table.

B. Method 2: Orthogonal image projection operator scheme

Method 2 did not use a reference image nor did it rely on the complex software used in Method 1 to locate the centers of the fringes and to interpolate their contours. Instead, this method used pairs of images taken at slightly different times, typically 6 or 12 s apart. The difference between the two images was computed, and the difference image was multiplied by an orthogonal image and by the eigenfunction of interest. The resulting array was spatially integrated to yield a scalar proportional to the amplitude of the image difference, projected onto the eigenfunction. This scalar was assumed to have the same exponential time dependence as that of the corresponding mode. This alternate method provided a valuable check on the results obtained with Method 1.

The intensity fields in the interferograms could be described by the general form

$$I_i(\mathbf{r}) = E_i(\mathbf{r}) + F_i(\mathbf{r}) \cos[\phi_i(\mathbf{r})], \quad (5.8)$$

where $i=1$ and 2 for the two images at times t_1 and t_2 , and $\phi_i(\mathbf{r})$ is the optical phase shift. In principle, the functions $E_i(\mathbf{r})$ and $F_i(\mathbf{r})$ could account for artifacts such as nonuniform illumination of the sample. In practice, we approximated these functions by the constants E and F . Thus, to analyze the difference between $I_1(\mathbf{r})$ and $I_2(\mathbf{r})$, we let

$$\begin{aligned} I_2 &= E + F \cos[\phi_1(\mathbf{r}) + \delta\phi(\mathbf{r})] \\ &= E + F \cos[\phi_1(\mathbf{r})] \cos[\delta\phi(\mathbf{r})] \\ &\quad - F \sin[\phi_1(\mathbf{r})] \sin[\delta\phi(\mathbf{r})]. \end{aligned} \quad (5.9)$$

Relying on the small angle approximation for $\delta\phi(\mathbf{r})$, the fluid-induced change between the two images was

$$I_1(\mathbf{r}) - I_2(\mathbf{r}) \cong F \delta\phi(\mathbf{r}) \sin[\phi_1(\mathbf{r})]. \quad (5.10)$$

From one of the two images, say $I_1(\mathbf{r})$, we generated an image $D(\mathbf{r})$, which was orthogonal in the sense that

$$\int I_1(\mathbf{r}) D(\mathbf{r}) d^2r = 0. \quad (5.11)$$

TABLE IV. The time constants τ_{ab} (in seconds) for various modes. Entries denoted by * have been corrected to account for the thermal conductivity of the sapphire windows. Entries denoted by † are affected by time-dependent temperature gradients in the sample cell unit.

Event	$T - T_c$ (mk)	τ_{11c}	τ_{11s}	τ_{21c}	τ_{21s}	τ_{31c}	τ_{31s}	τ_{12c}	τ_{12s}	τ_{13c}	τ_{13s}	τ_{tilt}	τ_0
<i>a</i>	198.2	198						146	207	233		179	138
<i>b</i>	198.2	124	375	111				302	150	133		180	219
<i>c</i>	98.6	400	403					358	360	318	317	373	332
<i>d</i>	98.6	408	413	380	385			360	366	306	318	404	348
<i>e</i>	98.6	405	409	380	377			371	367	320	332	390	331
<i>f</i>	98.4	422	463	456				405	322	365	354	441	420
<i>g</i>	48.4		859	807	728		677		765				678
<i>h</i>	28.4	1075	1141	1038	993			967	961	799	854	1087	883
<i>i</i>	28.7	1098	1077	1055	968			963	942	851	813	1051	866
<i>j</i>	28.4	1111	1167	1038	1146			1017	1052	821	901	1078	899
<i>k</i>	28.4	1194		1147		1068			1071				975
<i>l</i>	8.4	2670	2710	2840	2270			2340	2360	2040	2050	2740	2340
<i>m</i>	8.6	2500	2320	2070	2340			2210	2330	2180	2010	2400	2040
<i>n</i>	8.5	2660	2770	2300	2350			2420	2420	2120	2220	2510	1950
<i>o</i>	8.4		2370	2270	2350		2250		2250		1940		2530
<i>p</i>	3.4	5600	5470	5020	4350			4930	4630	4390	4060	5440	3970
* <i>p</i>	3.4	*5120†	*5010†	*4710	*4080			*4720†	*4430†	*4290†	*3960†		
<i>q</i>	1.4	15110	13630	11500	10130	7500	10360		19260				9230
* <i>q</i>	1.4	*13110†	*11830†	*10380	*9140	*6940	*9580		*17970†				

To obtain $D(\mathbf{r})$, we first performed a Fourier transform on $I_1(\mathbf{r})$ to obtain $\tilde{I}_1(\mathbf{k})$. We then defined

$$\tilde{D}(\mathbf{k}) \equiv \begin{cases} \tilde{I}_1(\mathbf{k}) & \text{if } k_y \geq 0 \\ 0 & \text{if } k_y < 0 \end{cases}. \quad (5.12)$$

The orthogonal image $D(\mathbf{r})$ was then obtained as the imaginary part of the inverse of $\tilde{D}(\mathbf{k})$.

To obtain a useful form of $D(\mathbf{r})$, we assumed that the fluid-induced phase shift $\delta\phi_1(\mathbf{r})$ and the spatial variations of $E_i(\mathbf{r})$ and $F_i(\mathbf{r})$ were small compared to the phase shift from the interferometer's reference mirror. Then

$$D(\mathbf{r}) \cong \frac{1}{2} F \sin[\phi_1(\mathbf{r})]. \quad (5.13)$$

We could then write the projection integral of the image differences as

$$P_1 - P_2 = \int d^2r [I_1(\mathbf{r}) - I_2(\mathbf{r})] D(\mathbf{r}) J_a(k_{ab}r) \begin{cases} \sin(a\theta) \\ \cos(a\theta) \end{cases} d^2r. \quad (5.14)$$

We fit $P_1 - P_2$ by the function $A \exp(-t/\tau_{ab})$ to obtain the time constant of the mode (a, b).

Table V compares the results for the J_{11} mode when three events were analyzed by both methods in a consistent man-

TABLE V. Comparison of Methods 1a and 2.

Event	$(T - T_c)$ (mK)	τ_{11} (s) (Method 1a)	τ_{11} (s) (Method 2)
<i>d</i>	98.6	411±4	463±5
<i>h</i>	28.4	1103±9	1107±15
<i>n</i>	8.5	2675±17	2478±32

ner. (The sine and cosine results are averaged to yield a single time constant τ_{11} .) The uncertainties listed are the standard deviations of the fits to the time dependence. They do not account for any other uncertainties. For events *d* and *n*, the two methods disagreed. However, the disagreement was smaller than the scatter among multiple measurements made at the same temperature. (See Table IV.)

Method 2 was unable to separate the (11), (12), and (13) modes, all of which have the same angular dependence. This was attributed to the approximations of the illumination fields $E(\mathbf{r})$ and $F(\mathbf{r})$ in Eq. (5.8) by constants. In reality, the illuminations varied by as much as a factor of 2 across an image. Because of this difficulty with Method 2, we used Method 1 in our final analysis.

C. Method 3: rms deviations

In Method 3, as in Method 1, a sequence of phase difference maps was obtained by subtracting the final reference phase map from the preceding phase maps. The rms deviation of each phase difference map was then calculated, and the tabulated data were then fit by an exponential decay to yield an effective time constant.

Method 3 was used only during the IML-2 mission to obtain a quick estimate of the experimental time constants. It assumed that the time dependence of the relaxation was that of a single exponential decay. According to our model, this assumption was only approximately true because it holds only in the limit of a disk of infinitesimal aspect ratio z_0/R . The strength of Method 3 was that it made no assumption about the spatial dependence of the density distribution. The results of Method 3 agreed to within 30% with those of Methods 1 and 2.

VI. RESULTS

With the possible exception of event q at $T_c + 1.4$ mK, the data were analyzed at times sufficiently long after the event that exponentially decaying density inhomogeneities were expected. As Fig. 5 shows, the amplitudes of the modes are fit well by exponential decays.

The ratios of the initial amplitudes of the various modes depended strongly on the method used to disturb the fluid. In particular, the amplitudes created by heating from an initial two-phase state to a one-phase state differed greatly from the amplitudes created by asymmetric heating of an initial, uniform, one-phase state. However, we saw no effect on the time constants.

A. Comparison with light scattering measurements of D_T

We tested our understanding of equilibration by comparing the present values of D_T with those measured by others. We used the relation

$$D_T = \frac{4z_0^2}{\pi^2 \tau_{ab}} \left[1 + \frac{4(j_{ab}^2 + a^2)}{\pi^2} \left(\frac{z_0}{R} \right)^2 \right]^{-1} \quad (6.1)$$

to calculate D_T from each of the 4–7 time constants τ_{ab} measured from each event. We averaged the D_T values from each event, and used the root-mean-square deviation of these values from their mean as a measure of their uncertainty. The error bars placed on selected points in Fig. 6 indicate this rms deviation. Figure 6 also includes values of D_T deduced from light scattering by Feke *et al.* [23] and Jany and Straub [24,25]. In the temperature range where the present measurements and the light scattering data overlap, the agreement between the present measurements and the data of Feke *et al.* is better than the agreement between the two sets of light-scattering data.

This is expected since the data of Feke *et al.* were taken at a smaller angle (4°) than those of Jany and Straub (8° – 10°). Although both papers calculated diffusivity by dividing the measured fluctuation decay rate by the square of the scattering wave vector, the smaller wave vector of Feke *et al.* made their apparent diffusivity a better approximation to the hydrodynamic (the wave vector goes to zero) diffusivity. (The lower values of Jany and Straub's data within 30 mK of T_c are consistent with an error of 5 mK in $T - T_c$, less than the 10-mK precision of the data [24].)

B. Correction for the cell's finite thermal conductivity

For the data closest to T_c , we applied a correction to Eq. (6.1) which accounted for heat currents in the cell's walls driven by the fluid's relaxation. Near T_c , these currents were large enough to induce a temperature gradient in the sapphire windows. The divergence of thermal conductivity near the liquid-vapor critical point makes this effect important close to T_c . The correction was calculated analytically by approximating the sapphire windows as cylinders of radius R and infinite thickness. At the boundary $r=R$, the temperature of both the fluid and the sapphire was held constant. At the boundaries $z = \pm z_0$, the temperature fields of the fluid and the sapphire were matched. The solution yielded the cor-

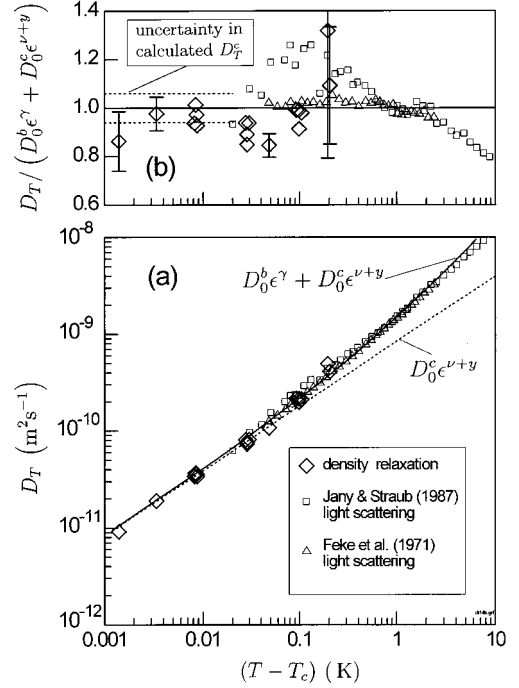


FIG. 6. (a) Experimental and calculated values of the thermal diffusivity D_T . The dashed line was calculated from the asymptotic term, Eq. (6.10), and the solid line was calculated from Eq. (6.11), which includes the asymptotic term and a correction term. Neither term has adjustable parameters. The present results are the mean values of D_T derived from the time constants τ_{ab} listed in Table IV, excluding gradient-affected data (τ_{1b} for events p and q). (b) The ratio of the data to D_T calculated with Eq. (6.11). The dashed lines indicate the calculated diffusivity's 6% uncertainty. The error bars indicate the rms deviations of the values of D_T from their mean.

rected time constant $\tilde{\tau}_{ab}$. Its value was greater than that of the uncorrected time constant τ_{ab} by the ratio

$$\frac{\tilde{\tau}_{ab}}{\tau_{ab}} = \frac{(\pi/2)^2 + j_{ab}^2 (z_0/R)^2}{(\tilde{q}z_0)^2 + j_{ab}^2 (z_0/R)^2}, \quad (6.2)$$

where the wave vector \tilde{q} is given by

$$(\tilde{q}z_0) \tan(\tilde{q}z_0) = j_{ab} (z_0/R) \left(\frac{\lambda_{\text{sapphire}}}{\lambda_{\text{SF}_6}} \right). \quad (6.3)$$

Here the thermal conductivity of sapphire is given by $\lambda_{\text{sapphire}} = 40 \text{ W m}^{-1} \text{ K}^{-1}$ [26]. The greatest correction was for the mode $ab = (11)$ at $T_c + 1.4$ mK. At this temperature we estimated λ_{SF_6} according to

$$\begin{aligned} \lambda_{\text{SF}_6} &= \rho c_p D_T \\ &\approx \left[\left(\frac{P_c}{T_c} \right) \left(\frac{T_c}{P_c} \frac{\partial P}{\partial T} \right)_{\rho_c}^2 (\Gamma \epsilon^{-\gamma}) \right] D_T \approx 1.2 \text{ W m}^{-1} \text{ K}^{-1}, \end{aligned} \quad (6.4)$$

and the resulting calculated ratio was $\tilde{\tau}_{11}/\tau_{11} = 1.15$. The τ_{ab} in Table IV which are marked by * have been reduced by the correction factors from their apparent values $\tilde{\tau}_{ab}$.

TABLE VI. Properties of SF₆ used to extrapolate D_T towards T_c .

Property	Value	Reference
T_c	(318.769±0.003) K	[this work]
P_c	3.76×10^6 Pa	[10]
ρ_c	(730±7) kg m ⁻³	[10,31]
ξ_0	$(1.88 \pm 0.06) \times 10^{-10}$ m	[32,33]
Γ	0.046	[10]
$(T_c/P_c)(\partial P/\partial T)_{\rho_c}$	6.8	[20]
λ^b	$0.021 \text{ W m}^{-1} \text{ K}^{-1}$	[30]
η_0	$(3.99 \pm 0.04) \times 10^{-5}$ Pa s	[29]
$(Q_0 \xi_0)^{-y/\nu}$	1.30 ± 0.04	[38]
R_D	1.00 ± 0.04	[36,13]

C. Exclusion of data affected by the thermostat's time-dependent temperature gradient

Temperature gradients $(dT/dx)_{\text{SCU}}$ in the SCU that were independent of time would not have affected the apparent relaxation times because the associated density gradients were subtracted using the reference image. In contrast, the time dependence of the thermostat's temperature gradient $(d\dot{T}/dx)_{\text{SCU}}$ limited the accuracy of the data close to T_c . Within 4 mK of T_c , the relaxation rate of the fluid's temperature gradient $(d\dot{T}/dr)_{\text{fluid}}$ across the cell's diameter was small enough to be comparable to $(d\dot{T}/dx)_{\text{SCU}}$. Under this condition, the effects of $(d\dot{T}/dx)_{\text{SCU}}$ are comparable to the relaxation of fluid modes.

The importance of this effect is demonstrated by comparing $(d\dot{T}/dx)_{\text{SCU}}$ with $(d\dot{T}/dr)_{\text{fluid}}$ for event q at $T_c + 1.4$ mK. During the analysis interval, the fluid mode proportional to $J_1(k_{11}r)\cos(\theta)$ had an initial amplitude $\delta T \approx 3 \mu\text{K}$, and it relaxed with an apparent time constant of $\tau_{11} \approx 1.4 \times 10^4$ s. The characteristic relaxation rate of the fluid's temperature gradient across the cell's diameter was thus $(d\dot{T}/dr)_{\text{fluid}} = \delta T / (R \tau_{11}) = 4 \times 10^{-8} \text{ K m}^{-1} \text{ s}^{-1}$, which is only twice the rate $(d\dot{T}/dx)_{\text{SCU}} = 2 \times 10^{-8} \text{ K m}^{-1} \text{ s}^{-1}$ inferred from the auxiliary thermistors during the same interval. (See Sec. III B)

If the gradient $(dT/dx)_{\text{SCU}}$ is linear in x , the only modes that are affected by its time dependence are those proportional to either $J_1(k_{1b}r)\sin(\theta)$ or $J_1(k_{1b}r)\cos(\theta)$. When deriving the thermal diffusivity D_T for events p and q , we excluded the time constants τ_{1b} . The exclusion reduced the normalized rms deviation of D_T from 0.25 to 0.14 for event q .

D. Comparison with extrapolations of D_T

Table VII lists the present measurements of D_T , which are averages of the D_T values derived from each event's time constants τ_{ab} . The τ_{ab} were corrected for the cell's finite conductivity as indicated in Table IV, and the gradient-affected data (τ_{1b} for events p and q) were excluded from the final averages.

At temperatures $T - T_c < 20$ mK, there are no prior measurements of D_T of SF₆. Therefore we compared our data at $T - T_c = 1.4, 3.4,$ and 8.5 mK with an extrapolation of $D_T(\epsilon)$, where $\epsilon \equiv (T - T_c)/T_c$ is the reduced temperature. An

asymptotically correct extrapolation can be found in Ref. [27]. One assumes that D_T can be separated into a background part D_T^b and a critical part D_T^c [28],

$$D_T \equiv D_T^b + D_T^c \equiv \frac{\lambda^b}{\rho c_P} + \frac{\lambda^c}{\rho c_P}, \quad (6.5)$$

where λ^b and λ^c are the background and critical parts of the thermal conductivity. Far from the critical point, one requires complicated expressions for c_P and λ^c to describe the ‘‘crossover’’ between the noncritical and critical regions. However, for the present purpose, we simply used the asymptotic forms for both terms.

The background term is

$$(D_T^b)_{T \rightarrow T_c} = \left(\frac{T_c \lambda^b}{\Gamma P_c} \right) \left[\frac{T}{P} \frac{\partial P}{\partial T} \right]_{\rho_c}^{-2} \epsilon^\gamma, \quad (6.6)$$

where P_c is the critical pressure, Γ is the amplitude for the reduced susceptibility, and γ is the associated universal exponent. The critical term of Eq. (6.5) is

$$(D_T^c)_{T \rightarrow T_c} = \frac{R_D k_B T_c}{6 \pi \eta \xi}, \quad (6.7)$$

where R_D is a universal constant, k_B is Boltzmann's constant, η is the viscosity, and ξ is the correlation length for microscopic density fluctuations. Substitution of the asymptotic forms for the viscosity

$$(\eta)_{T \rightarrow T_c} = \eta_0 (Q_0 \xi_0)^{y/\nu} \epsilon^{-y}, \quad (6.8)$$

and the correlation length

$$(\xi)_{T \rightarrow T_c} = \xi_0 \epsilon^{-\nu}, \quad (6.9)$$

gives

$$(D_T^c)_{T \rightarrow T_c} = \frac{R_D k_B T_c (Q_0 \xi_0)^{-y/\nu}}{6 \pi \eta_0 \xi_0} \epsilon^{\nu+y}. \quad (6.10)$$

Here ξ_0 is the correlation length amplitude, η_0 is the background viscosity, Q_0 is a characteristic wave vector, and the exponents $\nu=0.63$ and $y=0.04$ are universal exponents for the correlation length and viscosity, respectively.

The data used to determine $(D_T^b)_{T \rightarrow T_c}$ and $(D_T^c)_{T \rightarrow T_c}$ are listed in Table VI. The background viscosity η_0 was calculated by interpolating Hoogland, van den Berg, and Trappe-niers' viscosity measurements [29] made in a density range which included ρ_c . We adjusted the value measured at $T_c + 14$ K to that expected at T_c by using Table III of Ref. [29]. The result is $\eta_0 = (39.9 \pm 0.4) \mu\text{Pa s}$. We assigned a 1% uncertainty to η_0 due to the 1% rms scatter in the values of ρ_c reported in Ref. [31]. The correlation length amplitude ξ_0 is Cannell's value [32] adjusted by Moldover [33] for consistency with $\nu=0.63$. The 3% uncertainty in ξ reflects Cannell's assessment that his measurements of ξ had an accuracy of ‘‘a few percent.’’ Because the exponent $y/\nu \approx 0.06$ is so small, the quantity $(Q_0 \xi_0)^{-y/\nu}$ is expected to vary little from fluid to fluid. It is 1.28 for xenon, and 1.32 for CO₂. For SF₆

TABLE VII. Measured thermal diffusivities.

Event	$(T-T_c)$ (mK)	D_T (10^{-11} m ² s ⁻¹)
<i>a</i>	198.2	41.1±9.1
<i>b</i>	198.2	50.±20.
<i>c</i>	98.6	21.58±0.37
<i>d</i>	98.6	21.56±0.30
<i>e</i>	98.6	21.35±0.60
<i>f</i>	98.4	19.85±1.98
<i>g</i>	48.4	10.77±0.62
<i>h</i>	28.4	8.10±0.23
<i>i</i>	28.7	8.15±0.23
<i>j</i>	28.4	7.68±0.30
<i>k</i>	28.4	7.32±0.03
<i>l</i>	8.4	3.41±0.20
<i>m</i>	8.6	3.65±0.32
<i>n</i>	8.5	3.40±0.22
<i>o</i>	8.4	3.69±0.14
<i>p</i>	3.4	1.90±0.14
<i>q</i>	1.4	0.92±0.14

we used the value 1.30 ± 0.04 , where the uncertainty is an estimate based on the availability of only two values [34,35].

The largest uncertainty in D_T^c comes from the factor R_D . Burstyn *et al.* [36] analyzed data from light scattering in the liquid mixture nitroethane plus 3-methylpentane [37], and found $R_D = 1.01\pm 0.03$. Berg and Moldover [13] combined their new, accurate viscosity data [38] with Güttinger and Cannell's light-scattering data in xenon [39,40] to find $R_D = 0.99\pm 0.03$. Here the uncertainty of $\pm 3\%$ was assigned to be similar to that for Cannell's measurement of ξ [32]. (Güttinger and Cannell's original assignment of 5% included the uncertainty of the older viscosity data.) Consistent with these two experimental determinations, we used the value $R_D = 1.00\pm 0.04$. This value is lower than the various theoretical calculations of R_D discussed in Ref. [27], which varied from 1.03 to 1.20.

Equation (6.5) has the asymptotic form

$$(D_T)_{T\rightarrow T_c} = D_0^b \epsilon^{1.24} + D_0^c \epsilon^{0.63+0.04}, \quad (6.11)$$

where $D_0^b = 1.32 \times 10^{-6}$ m² s⁻¹, $D_0^c = (4.05 \pm 0.24) \times 10^{-8}$ m² s⁻¹, and the uncertainty in D_0^c is the sum in

quadrature of the uncertainties discussed above. For $T < T_c + 20$ mK, the background term of Eq. (6.11) is so small that the uncertainty of $(D_T)_{T\rightarrow T_c}$ is determined solely by that of D_0^c . Figure 6 compares the present data to $(D_T)_{T\rightarrow T_c}$ calculated from Eq. (6.11). Our data at $T - T_c = 1.4, 3.4,$ and 8.5 mK agree with the extrapolation of D_T to within the combined uncertainties of our data and of D_0^c .

VII. CONCLUSIONS

The present results support our quantitative understanding of the late stage of equilibration of one-phase states near the liquid-vapor critical point. First, the amplitudes of the thermal modes decayed exponentially in time. Second, although the method used to disturb the fluid greatly influenced the initial spatial dependence of the density, it did not affect the measured time constants. In other words, the time constants depended only on reduced temperature, and not on the sample's history. Third, the values inferred for the thermal diffusivity D_T are consistent with published light scattering measurements, and they agree with an asymptotically correct extrapolation close to T_c .

On Earth, gravity's complications have prevented a definitive test of the understanding of late-stage equilibration near the liquid-vapor critical point. The present work has experimentally confirmed this understanding at temperatures as close to T_c as 1.4 mK.

ACKNOWLEDGMENTS

This experiment was made possible by the Critical Point Facility, originally conceived by A. Michels of the Van der Waals Laboratory in Amsterdam. The construction and management of CPF was funded by the European Space Agency. Principal participants were D. Hüser, B. Jähn, and their DASA-RI/ERNO team, and M. Cork and T. DeWandre of ESA/ESTEC. R. Kusner, A. DeGennaro, M. Bayda, and H. Nahra supported mission planning and operations. We received much stimulation from Professor J. Straub, who collaborated on the original experiment TEQ. We also wish to thank the IML-2 crew and the mission support staff at Marshall Space Flight Center, all of whom helped make this a successful microgravity experiment. This work was supported in part by NASA under Grant No. NAG3-1395.

-
- [1] H. Boukari, J. N. Shaumeyer, M. E. Briggs, and R. W. Gammon, *Phys. Rev. A* **41**, 2260 (1990).
[2] A. Onuki, H. Hao, and R. A. Ferrell, *Phys. Rev. A* **41**, 2256 (1990).
[3] A. Onuki and R. A. Ferrell, *Physica A* **164**, 245 (1990).
[4] H. Boukari, M. E. Briggs, J. N. Shaumeyer, and R. W. Gammon, *Phys. Rev. Lett.* **65**, 2654 (1990).
[5] H. Klein, G. Schmitz, and D. Woermann, *Phys. Rev. A* **43**, 4562 (1991).
[6] F. Zhong and H. Meyer, in AMD-Vol. 174, *Fluid Mechanics Phenomena in Microgravity*, edited by D. A. Siginer, R. L. Thompson, and L. M. Trefethen (ASME, New York, 1993), p. 139; *Phys. Rev. E* **51**, 3223 (1995).
[7] M. Bonetti, F. Perrot, D. Beysens, and Y. Garrabos, *Phys. Rev. E* **49**, 4779 (1994).
[8] J. Straub, L. Eicher, and A. Haupt, *Phys. Rev. E* **51**, 5556 (1995).
[9] T. Fröhlich, P. Guenoun, M. Bonetti, F. Perrot, and D. Beysens, *Phys. Rev. E* **54**, 1544 (1996).
[10] M. R. Moldover, J. V. Sengers, R. W. Gammon, and R. J. Hocken, *Rev. Mod. Phys.* **51**, 79 (1979).
[11] H. Meyer (private communication).
[12] F. Zhong, A. Kogan, and H. Meyer, *J. Low Temp. Phys.* **108**, 161 (1997).

- [13] R. F. Berg and M. R. Moldover, Science Requirements Document, report to NASA Lewis Research Center, Report No. 60009-DOC-006, 1993; R. F. Berg (unpublished).
- [14] R. F. Berg, *Phys. Rev. E* **48**, 1799 (1993).
- [15] R. A. Ferrell, R. A. Wilkinson, and H. Hao, *Phys. Rev. E* (to be published).
- [16] W. Rathjen and J. Straub, in *Proceedings of the Seventh Symposium on Thermophysical Properties*, edited by A. Cezairliyan (ASME, New York, 1977), p. 839.
- [17] T. Dewandre, *Critical Point Facility (CPF) User's Guide* (European Space Research and Technology Centre, Noordwijk, 1991); M. Cork, T. Dewandre, and D. Hüser, *Space Agency Bul.* 74 (1993).
- [18] A. Michels (private communication).
- [19] C. M. Vest, *Holographic Interferometry* (Wiley, New York, 1979), p. 329.
- [20] S. N. Biswas, N. J. Trappeniers, and J. H. B. Hoogland, *Physica A* **126**, 384 (1984).
- [21] FAST VAI, Phase Shift Technology, Tucson, 1992.
- [22] In order to describe materials and experimental procedures adequately, it is occasionally necessary to identify commercial products by manufacturers' name or label. In no instance does such identification imply endorsement by the National Institute of Standards and Technology, nor does it imply that the particular product or equipment is necessarily the best available for the purpose.
- [23] G. T. Feke, G. A. Hawkins, J. B. Lastovka, and G. B. Benedek, *Phys. Rev.* **26**, 1780 (1971).
- [24] P. Jany, doctoral Dissertation, Technische Universität München, 1986 (unpublished).
- [25] P. Jany and J. Straub, *Int. J. Thermophys.* **8**, 165 (1987).
- [26] G. E. Childs, L. J. Ericks, and R. L. Powell, *Thermal Conductivity of Solids at Room Temperature and Below*, National Bureau of Standards Monograph No. 131 (NBS, Washington, D.C., 1973).
- [27] J. Luettmmer-Strathmann, J. V. Sengers, and G. A. Olchoway, *J. Chem. Phys.* **103**, 7482 (1995).
- [28] J. V. Sengers and P. H. Keyes, *Phys. Rev. Lett.* **26**, 70 (1971).
- [29] J. H. B. Hoogland, H. R. van den Berg, and N. J. Trappeniers, *Physica A* **134**, 169 (1985).
- [30] J. Lis and P. O. Kellard, *Br. J. Appl. Phys.* **16**, 1099 (1965).
- [31] K. Watanabe, H. Watanabe, and K. Oguchi, in *Proceedings of the Seventh Symposium on Thermophysical Properties*, edited by A. Cezairliyan (ASME, New York, 1977), p. 489.
- [32] D. S. Cannell, *Phys. Rev. A* **12**, 225 (1975).
- [33] M. R. Moldover, *Phys. Rev. A* **31**, 1022 (1985).
- [34] *Standard Mathematical Tables and Formulae*, edited by D. Zwillinger (CRC, Boca Raton, FL, 1996), Sec. 7.8.1.2.
- [35] E. B. Wilson, in *Introduction to Scientific Research* (McGraw-Hill, New York, 1952), p. 239.
- [36] H. C. Burstyn, J. V. Sengers, J. K. Bhattacharjee, and R. A. Ferrell, *Phys. Rev. A* **28**, 1567 (1983).
- [37] H. C. Burstyn and J. V. Sengers, *Phys. Rev. A* **25**, 448 (1982).
- [38] R. F. Berg and M. R. Moldover, *J. Chem. Phys.* **93**, 1926 (1990).
- [39] H. Güttinger and D. S. Cannell, *Phys. Rev. A* **22**, 285 (1980).
- [40] D. S. Cannell (private communication).